



## Boron-doped rGO electrocatalyst for high effective generation of hydrogen peroxide: Mechanism and effect of oxygen-enriched air

KwangChol Ri <sup>a,b</sup>, SongSik Pak <sup>a,b</sup>, Dunyu Sun <sup>a</sup>, Qiang Zhong <sup>a</sup>, Shaogui Yang <sup>a,c,\*</sup>, SongIl Sin <sup>a,d</sup>, Leliang Wu <sup>a</sup>, Yue Sun <sup>a</sup>, Hui Cao <sup>a</sup>, Chunxiao Han <sup>a</sup>, Chenmin Xu <sup>a</sup>, Yazi Liu <sup>a</sup>, Huan He <sup>a</sup>, Shiyin Li <sup>a</sup>, Cheng Sun <sup>e</sup>

<sup>a</sup> School of Environment, Jiangsu Province Engineering Research Center of Environmental Risk Prevention and Emergency Response Technology, Jiangsu Engineering Lab of Water and Soil Eco-remediation, Nanjing Normal University, Nanjing, Jiangsu 210023, People's Republic of China

<sup>b</sup> Institute of Chemical Engineering, Hamhung University of Chemical Engineering, Hamhung, Democratic People's Republic of Korea

<sup>c</sup> Suzhou Furong Environmental Engineering Co., Ltd, Suzhou 215500, People's Republic of China

<sup>d</sup> Department of Mining Engineering, Kim Chaek University of Technology, Pyongyang, Democratic People's Republic of Korea

<sup>e</sup> State Key Laboratory of Pollution Control and Resource Reuse, School of Environment, Nanjing University, Nanjing, Jiangsu 210023, People's Republic of China



### ARTICLE INFO

#### Keywords:

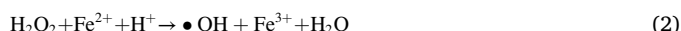
Boron-doped rGO  
Hydrogen peroxide  
Oxygen reduction reaction  
Electro-Fenton  
Organic pollutant

### ABSTRACT

Different B-doped rGO catalysts were prepared and their  $2e^-$  oxygen reduction reaction (ORR) performance was investigated. It was found that the  $2e^-$  ORR selectivity of B-doped rGO was related to the B content and oxygen mass transfer conditions. The synthesized catalyst exhibited high  $2e^-$  ORR selectivity of 95–98.6%, and the  $H_2O_2$  yield reached up to  $95.63 \text{ mg cm}^{-2} \text{ h}^{-1}$  at a current density of  $200 \text{ mA cm}^{-2}$ . Moreover, increasing the oxygen concentration in the gas supplied to the B-doped rGO modified gas diffusion electrode (GDE) only to 30–40% resulted in almost the same  $H_2O_2$  yield as using pure oxygen. Experimental analysis and theoretical calculations indicated that the isolated B dopant acts as active site for the  $2e^-$  ORR. Furthermore, B-doped rGO modified GDE was applied to the electro-Fenton system to continuously degrade organic pollutants. This work will be beneficial for the study and application of carbon-based ORR catalysts.

### 1. Introduction

Electro-Fenton (EF) technology is a promising method for the degradation of recalcitrant organic pollutants due to its high efficiency and environmental compatibility [1]. In EF technology, hydrogen peroxide ( $H_2O_2$ ) can be in situ produced at the cathode by a two-electron oxygen reduction reaction ( $2e^-$  ORR, Eq. (1)) [2–5], which reacts with  $Fe^{2+}$  to generate hydroxyl radicals (Eq. (2)) [6–8].



The current industrial-scale  $H_2O_2$  synthesis is mainly based on the anthraquinone process. This process requires expensive  $H_2$  and noble metal catalyst, toxic organic solvents, and high energy input [9]. The electrochemical synthesis of  $H_2O_2$  using a  $2e^-$  ORR has emerged as an attractive alternative for the continuous in situ production of  $H_2O_2$ . The

in situ electrochemical synthesis of  $H_2O_2$  also avoids hazardous storage and transportation processes, broadening its application for organic pollutant removal via the  $H_2O_2$ -based EF process [10]. Theoretically,  $O_2$  molecules will be chemically adsorbed on the active site of catalyst and form  $^*OOH$  intermediate during the initial activation stage [11,12]. And the adsorbed  $^*OOH$  species can directly escape from active site and form the target  $H_2O_2$  product through next step electron transfer [3,13]. However, depending on its adsorption configuration and corresponding intensity, the  $^*OOH$  species can simultaneously generate  $H_2O$  byproduct through the  $4e^-$  ORR, resulting in the sharp decrease of  $H_2O_2$  yield [13,14]. Therefore, enhancing the  $2e^-$  ORR performance of the catalyst is a core challenge. Generally speaking, catalyst selectivity and oxygen mass transfer are important factors that affect the  $H_2O_2$  yield [15–17].

Noble metals such as platinum and its alloys exhibit excellent  $2e^-$  ORR selectivity, however, the high cost and scarcity of noble metals make it difficult for large-scale application [13]. Carbon materials can be used as ORR catalysts to replace noble metals owing to their abundant

\* Corresponding author at: School of Environment, Jiangsu Province Engineering Research Center of Environmental Risk Prevention and Emergency Response Technology, Jiangsu Engineering Lab of Water and Soil Eco-remediation, Nanjing Normal University, Nanjing, Jiangsu 210023, People's Republic of China.

E-mail address: [yangsg@njnu.edu.cn](mailto:yangsg@njnu.edu.cn) (S. Yang).

sources, excellent electrochemical properties, and environmental friendliness [3,5,13,18]. Nevertheless, pristine carbon materials exhibit low  $2e^-$  ORR selectivity [4,13], thus various methods such as heteroatom (O, N, F, S, P, B) doping are employed to improve their  $2e^-$  ORR selectivity [13]. It is reported that these non-metallic dopants can act as active sites or modify the electronic properties of the neighboring carbon atoms [5,13,19,20]. Especially, N and B are neighboring elements to C in the periodic table and can easily substitute C atoms in carbon materials [21]. Boron atom has a lower electronegativity than carbon, resulting in a positive charge after doping, this can facilitate the adsorption and reduction of oxygen molecules [19,22–24]. Therefore, a series of studies have been conducted to improve the ORR activity of carbon-based catalysts by B doping [5,19,20,22,23,25,26]. Unfortunately, the ORR active sites and reaction pathways of B-doped carbon materials are still unclear. On the one hand, B-doping enhances the  $2e^-$  ORR selectivity of carbon-based catalysts [19,20]. Xia et al. demonstrated that B-doped carbon materials have a very low overpotential for  $2e^-$  ORR through density functional theory (DFT) calculations and experimental analysis [19]. On the other hand, B-doped carbon materials can also promote  $4e^-$  ORR [25,26]. Vineesh et al. synthesized B-doped graphene and confirmed its excellent  $4e^-$  ORR selectivity ( $e^-/O_2 \approx 3.9$ ) [25]. These results show that different active sites catalyzing  $2e^-$  ORR or  $4e^-$  ORR can exist in B-doped carbon materials and the selectivity of the catalyst depends on the specific synthesis conditions (e.g., B content). The ORR selectivity of the catalyst has traditionally been described in terms of the thermodynamics of the surface-adsorbed intermediates [14], which may be different for different B species. Hence, it is an important task to investigate the ORR active sites and reaction pathways of B-doped carbon materials.

Moreover, besides the catalyst selectivity, the oxygen mass transfer is also a critical factor to control ORR, which could be limited by the low oxygen solubility in the electrolyte, resulting in the retarded kinetics of the  $2e^-$  ORR [1,15,27–29]. The oxygen solubility in the electrolyte is related to the oxygen content of the cathode gas, and when the oxygen content changes, the amount of dissolved oxygen in the electrolyte changes correspondingly [1,6]. And, it is unclear how these changes will affect the  $2e^-$  ORR activity or selectivity of the catalyst, and as far as we know, few studies have been reported. In addition, the oxygen mass transfer in the gas diffusion electrode (GDE) differs from the submerged electrode, and the oxygen is directly transferred to the active site through the three-phase interface without dissolving in the electrolyte [30]. It is well known that the hydrophobicity of the catalyst layer in GDE affects the formation of the three-phase interface and oxygen mass transfer [27,31]; however, the effect of the oxygen content of the gas supplied to the GDE has hardly been investigated.

In this work, to understand the  $2e^-$  ORR and  $4e^-$  ORR selective reaction mechanisms of B-doped carbon materials, we synthesized different B-doped rGOs and investigated ORR performance, and studied  $2e^-$  ORR catalytic active site of B-doped rGO by experimental analysis and DFT calculations. In addition, the effect of oxygen content in the cathode gas on the  $2e^-$  ORR performance of B-doped rGO was investigated. Finally, high-efficient continuous degradation of organic pollutants, such as rhodamine B (RhB), iohexol (IOH), acetaminophen (AAP), and tetracycline (TC), was achieved on a homogeneous EF system with B-doped rGO modified GDE. This work will offer new possibilities for the industrial scale-up of the EF process.

## 2. Experimental and calculation methods

### 2.1. Materials preparation

The detailed chemicals and materials used in this study are presented in **Text S1** of the **Supporting Information**. Graphite oxide (GO) was prepared from flake graphite via the modified Hummers method [32] (The details of method was provided in **Text S2**). Then, different amounts of boric acid (50, 100, 200, and 400 mg) were added to 50 mL

of GO dispersion ( $\sim 50$  mg) and stirred for 30 min. Here, the corresponding mass ratios of boric acid to GO were 1, 2, 4, and 8. The resulting mixtures were transferred to polytetrafluoroethylene (PTFE) autoclaves and hydrothermally treated at  $180^\circ\text{C}$  for 12 h to obtain hydrogels [20]. The obtained hydrogels were freeze-dried for 72 h and then annealed in an Ar-H<sub>2</sub> (H<sub>2</sub>: 5%) atmosphere in a tube furnace at various temperatures ( $600$ – $900^\circ\text{C}$ ) for 2 h to obtain B-doped rGO samples. The samples were denoted as xB-rGO-y, where x is the mass ratio of boric acid to GO, and y is the annealing temperature ( $^\circ\text{C}$ ). For example, when the mass ratio of boric acid to GO was 4 and the annealing temperature was  $800^\circ\text{C}$ , it was denoted as 4B-rGO-800. As a comparison, B-free rGO was also synthesized via the same process without adding boric acid.

### 2.2. Electrode fabrication

Carbon paper and carbon cloth were used as substrates for the fabrication of electrodes for electrochemical measurements and H<sub>2</sub>O<sub>2</sub> generation, respectively. The substrates were washed with acetone and deionized water in an ultrasonic bath and dried at  $120^\circ\text{C}$  for 2 h before use. In a typical fabrication process of catalyst modified carbon paper electrode, the B-doped rGO catalyst was dispersed in ethanol at a concentration of  $1\text{ mg mL}^{-1}$  by sonication for 20 min. Then, 2 mL of the catalyst dispersion was taken out under stirring, and 18  $\mu\text{L}$  of 5% PTFE emulsion was added to the catalyst dispersion and sonicated for another 20 min. Subsequently, the 100  $\mu\text{L}$  (when the catalyst loading mass is  $100\text{ }\mu\text{g cm}^{-2}$ ) or 200  $\mu\text{L}$  (when the catalyst loading mass is  $200\text{ }\mu\text{g cm}^{-2}$ ) of obtained catalyst-PTFE mixture was uniformly coated onto the carbon paper ( $1.0\text{ cm} \times 1.0\text{ cm}$ ) and dried at  $100^\circ\text{C}$  for 1 h. Finally, the carbon papers coated by catalyst-PTFE mixture were annealed in a muffle furnace at  $360^\circ\text{C}$  for 2 h to obtain the B-doped rGO catalyst modified electrode. The electrodes with an area of  $3\text{ cm}^2$  ( $2.0\text{ cm} \times 1.5\text{ cm}$ ) were used to investigate the selectivity of catalysts at different oxygen content. The GDEs for H<sub>2</sub>O<sub>2</sub> accumulation experiments were fabricated using carbon cloth ( $3.0\text{ cm} \times 1.0\text{ cm}$ ). The 9 mg of B-doped rGO catalyst was added to 3 mL of ethanol and sonicated for 20 min, then 11  $\mu\text{L}$  of 60% PTFE emulsion was added and sonicated for another 20 min. The obtained catalyst-PTFE mixture was uniformly coated onto the as-prepared carbon cloth, and annealed at  $360^\circ\text{C}$  for 2 h to obtain the GDEs.

### 2.3. Analysis methods

The details of the analysis methods were provided in **Text S3**.

### 2.4. Electrochemical measurements

The electrochemical performance of the catalysts was evaluated by electrochemical impedance spectra (EIS), cyclic voltammetry (CV), linear sweep voltammetry (LSV), and chronopotentiometry (CP) using an electrochemical workstation (SP-150, Bio-Logic SAS). The working electrode was catalyst modified carbon paper, and a Pt electrode ( $2.0\text{ cm} \times 1.5\text{ cm}$ ) and a saturated calomel electrode (SCE) were used as the counter and reference electrodes, respectively. The electrolyte was 0.05 M Na<sub>2</sub>SO<sub>4</sub> with 0.05 M H<sub>2</sub>SO<sub>4</sub> to adjust the pH value, which was determined by a SevenExcellence S470-K (METTLER TOLEDO). The potentials measured for the SCE were converted to the reversible hydrogen electrode (RHE) scale [19,33]. A three-electrode cell was used for EIS and CV to determine the electric double layer capacitance (EDLC) of the catalysts, and an H-cell with a Nafion membrane was used for LSV and CP to investigate the catalyst selectivity. The  $2e^-$  ORR selectivity of the prepared catalysts was evaluated by the number of electrons consumed per oxygen molecule ( $e^-/O_2$ ). To do this, oxygen consumption during the ORR was measured using sealed H-cell. This modified H-cell, which improves on McCloskey group's method [32,34], determines the oxygen consumption by the mass change of the electrolyte. (The details

of the configuration and methods were provided in Fig. S1 and Text S4. Unlike rotating disk electrode (RDE) or rotating ring disk electrode (RRDE), this method is insensitive to the surface roughness of the catalyst layer [32] and can examine the selectivity variation of the catalyst under different oxygen content.

RRDE measurements were also conducted for comparison. The catalyst ink was prepared by dispersing 1 mg of catalyst in 100  $\mu$ L of deionized water, 900  $\mu$ L of ethanol, and 10  $\mu$ L of nafton solution (5 wt %) and sonicated for 20 min. Then, 15  $\mu$ L of the ink was dropped on the disk and dried at room temperature [35]. The SCE and Pt sheet were used as the reference and counter electrodes, respectively. The ring potential was fixed at 1.2 V vs RHE, the electrode rotation speed was 1600 rpm, and the scan rate was 10 mV s<sup>-1</sup>.

## 2.5. Hydrogen peroxide accumulation and electro-Fenton experiments

$H_2O_2$  accumulation experiments were conducted in an unseparated 250 mL cylindrical glass reactor using the fabricated catalyst modified GDE. The cathode and anode areas were both 3 cm<sup>2</sup> and a programmable DC Power Supply (IT6922A, ITECH) was used for experiments. The experiments were conducted at room temperature ( $25 \pm 1$  °C) with 200 mL 0.05 M  $Na_2SO_4$  as the electrolyte, and the electrolyte was stirred at 600 rpm using a magnetic stirrer during the reaction. The  $H_2O_2$  concentration was detected by a UV-visible spectrophotometer using the iodide method [10,35,36] at 352 nm, and the details of iodide method and corresponding current efficiency (CE) calculation method were reported in Text S5 and S6. To control the oxygen content of the gas supplied to the GDE, pristine air and oxygen were mixed in a corresponding ratio, and the oxygen content was measured using an oxygen meter (JC-D2200, Jiachang electronics). The continuous degradation experiments were conducted using RhB, IOH, AAP, and TC as target pollutants, and the specific configuration and experimental methods were described in Fig. S25 and Text S7. The applied current density was 60 mA cm<sup>-2</sup>, the gas flow rate was 8 mL cm<sup>-2</sup> min<sup>-1</sup>, and the pH values of solution was adjusted to 3 by adding 0.05 M  $H_2SO_4$  solution, and no buffer solution was used. At regular time intervals, 0.8 mL of the reaction solution was taken out and filtered with a 0.22  $\mu$ m membrane filter and quenched with 0.2 mL methanol to terminate the reaction. The pollutant concentration was determined by UV-vis spectrophotometry or high-performance liquid chromatography (HPLC, 1260 Infinity, Agilent), and the respective measurement conditions and methods were

reported in Text S8. Total organic carbon (TOC) of the solutions was detected with a Jena multi-N/C 3100.

## 2.6. Theoretical calculations details

The methods for theoretical calculations were provided in Text S9.

## 3. Results and discussion

### 3.1. Materials characterization and electrochemical performance

Firstly, to investigate the effect of the amount of B dopant on the 2e<sup>-</sup> ORR electrocatalytic performance of the B-doped rGO catalyst, samples with different B content were prepared. Fig. 1a, 1b, 1e, and 1f show scanning electron microscopy (SEM) images of the prepared rGO and B-doped rGO. The samples were composed of disordered thin sheets. SEM and transmission electron microscopy (TEM) images show that the samples have a few-layered graphene morphology and form wrinkled sheets with partially folded or scrolled edges due to high surface tension [37]. The rGO and B-doped rGO sheets were mostly below 5  $\mu$ m in size. High-resolution TEM (HRTEM) images show that rGO and B-doped rGO have a planar structure with 5–15 layers, and the layer spacing was about 0.35–0.37 nm (Fig. 1 and Fig. S2). This layer spacing was slightly larger than that of pristine graphite (0.34 nm), which may be due to the presence of oxygen functional groups (OFG) in the rGO and B-doped rGO sheets [37]. No significant changes were observed in the morphology and nanostructure of rGO after B doping.

The high-resolution X-ray photoelectron spectroscopy (XPS) spectra (Fig. 2a, 2b, and Fig. S3) show that the B atoms were successfully doped with ratios of 0.51, 0.86, 1.12, and 1.59 at%. The peak of B-C species in the C1s spectrum of B-doped rGO was found at 283.8 eV [21,22,24,37]. The spectrum of B1s lies in the region of 188–195 eV and could be deconvoluted into five peaks with different intensities centered at 188.6, 189.8, 191.2, 192.7, and 193.4 eV [20,22,37–39]. The peak at 188.6 eV corresponds to boron carbide (B<sub>4</sub>C) [26,38,40], and the strong peak at 189.8 eV originates from B-sub-C [19,21,37,41,42]. B-sub-C species refers to the substitution of a C atom by a B atom in the graphene lattice, which includes a single C atom by a B atom (BC<sub>3</sub>) and two or more C atoms by B atoms (B<sub>2</sub>C<sub>4</sub> etc.), and it is difficult to distinguish them as specific peaks [37,43]. Isolated B atom (BC<sub>3</sub>) dominates in samples with low B content, while interconnected B atoms (B<sub>2</sub>C<sub>4</sub> etc.) dominates in

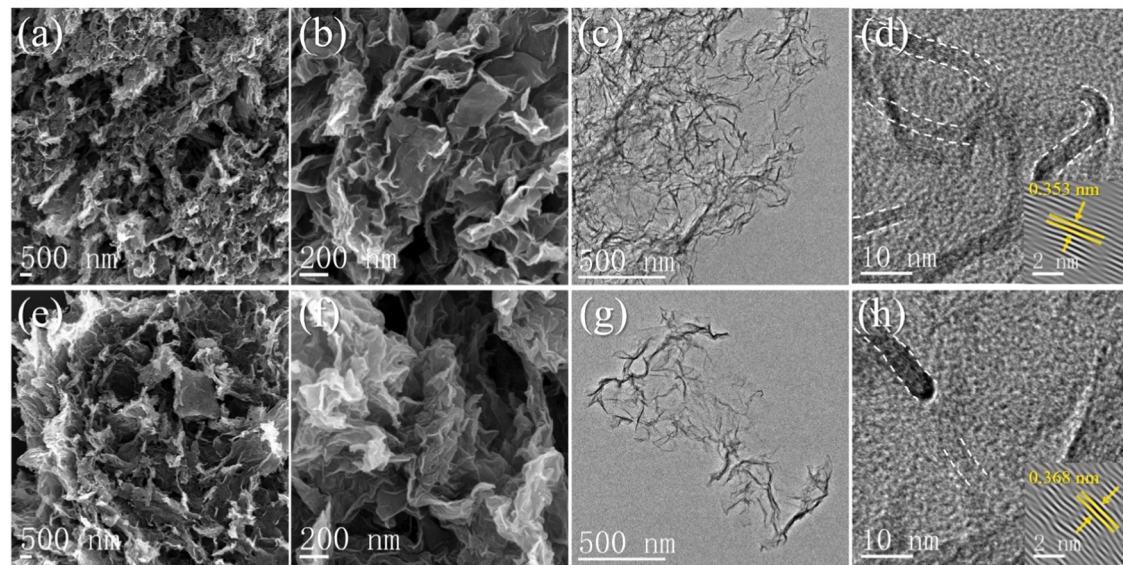


**Fig. 1.** (a, b) SEM, (c) TEM, and (d) HRTEM image of rGO. (Inset for the FFT image) (e, f) SEM, (g) TEM, and (h) HRTEM image of 4B-rGO-800. (Inset for the FFT image).

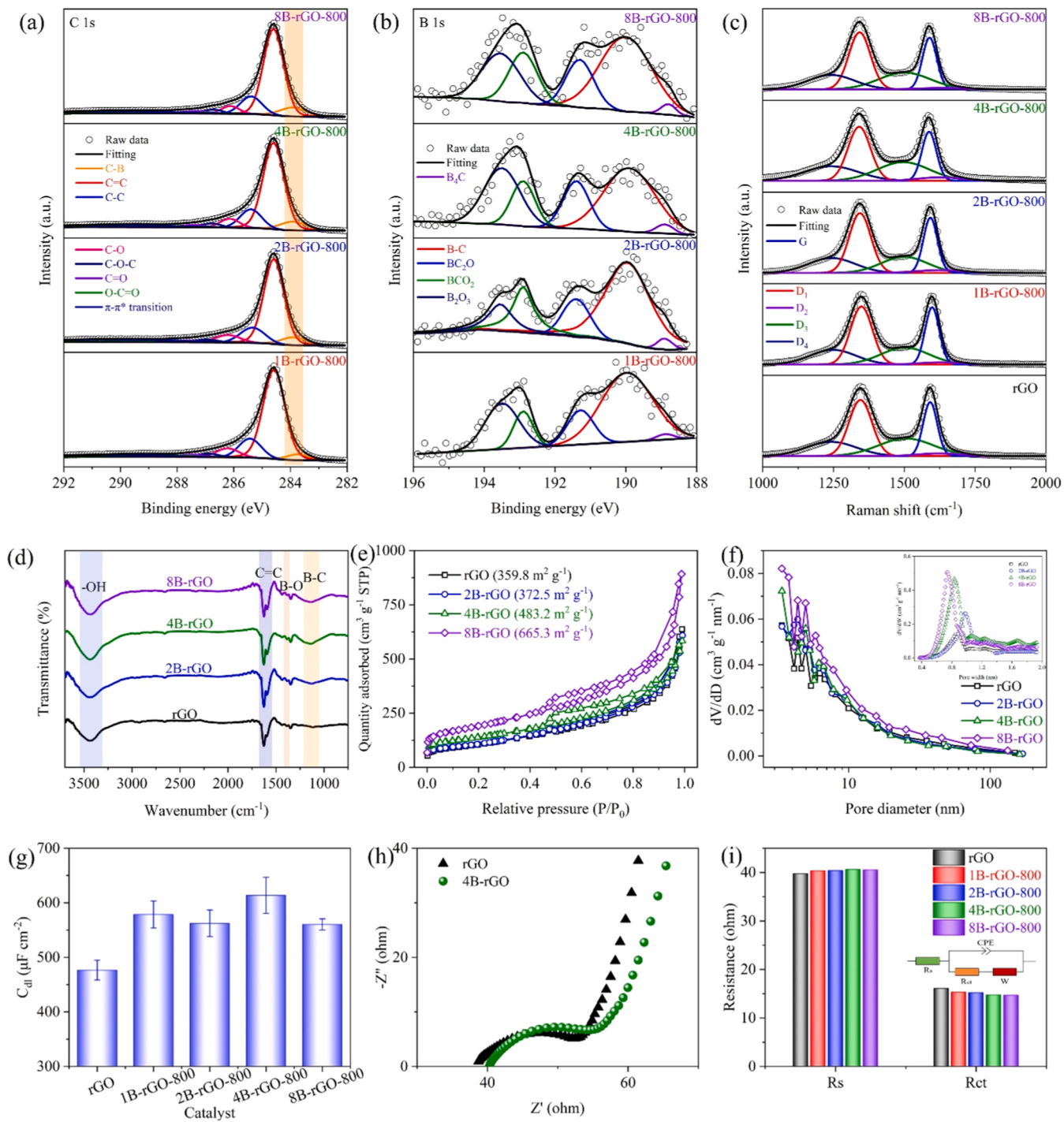


**Fig. 2.** (a, b) The XPS high-resolution C1s and B1s spectra of 1B-rGO-800, 2B-rGO-800, 4B-rGO-800 and 8B-rGO-800. (c) The deconvoluted Raman spectra of rGO, 1B-rGO-800, 2B-rGO-800, 4B-rGO-800 and 8B-rGO-800. (d) The FT-IR spectra of rGO, 2B-rGO-800, 4B-rGO-800 and 8B-rGO-800. (e) The  $N_2$  adsorption-desorption isotherms and (f) pore size distributions of rGO, 2B-rGO-800, 4B-rGO-800 and 8B-rGO-800. (g) The electric double layer capacitance (EDLC) measurements of rGO, 1B-rGO-800, 2B-rGO-800, 4B-rGO-800 and 8B-rGO-800 (catalyst loading mass:  $100 \mu\text{g cm}^{-2}$ ). (h) Nyquist plots, (i) the corresponding ohmic resistance and charge-transfer resistance.

samples with high B content [43]. The peaks at 191.2 eV and 192.7 eV could be ascribed to  $\text{BC}_2\text{O}$  [42,44,45] and  $\text{BCO}_2$  [22,26,45], respectively, and the peak at 193.4 eV could be attributed to boron oxide ( $\text{B}_2\text{O}_3$ ) [37,44]. The XPS spectra confirm the presence of B-C bonds, indicating that the C atoms in the graphene lattice were replaced by B atoms. In all samples, the amount of  $\text{B}_4\text{C}$  was a negligible fraction, less than 3% of the B dopant, and the ratios of B-sub-C were 67.5%, 62.6%, 56.9%, and 56.7%, respectively, which constituted the majority, and the

percentage of  $\text{BC}_2\text{O}$  and  $\text{BCO}_2$  showed an increasing trend with increasing B content. In addition, the O content was between 3.02% and 3.38% in all samples (Fig. S4).

Raman spectra were employed to analyze the presence of defects in rGO and B-doped rGO [20]. Many studies reported that structural defects in the graphene lattice increase its ORR activity [5,13,46–48]. As shown in Fig. 2c and Fig. S5, the samples all exhibited typical D and G bands at  $1350 \text{ cm}^{-1}$  and  $1580 \text{ cm}^{-1}$  [32,34]. The intensity ratio of the D

band to G band ( $I_D/I_G$ ) is commonly used to assess the level of disorder in carbon materials [32,49]. Fig. 2c and Table S1 show that  $I_{D1}/I_G$  slightly increases with the increase of B content. This indicates that the doping of B atoms can lead to structural defects and disorder in rGO [20]. Fourier transform infrared (FT-IR) spectroscopy is another powerful method for characterizing functional groups [50] and it has been used to analyze the B-doped rGO samples. Fig. 2d show the FT-IR spectra of the samples. All spectra exhibited a peak approximately at  $3400\text{ cm}^{-1}$ , which is mainly assigned to the stretching vibration of the water adsorbed on KBr [24,37, 51]. The peak at  $1625\text{ cm}^{-1}$  could be associated with contributions from O-H bending vibrations of the adsorbed water molecules and vibrations of the aromatic C=C [37]. The peaks observed in the regions of  $1383\text{ cm}^{-1}$  and  $1050\text{--}1200\text{ cm}^{-1}$  correspond to B-O and B-C stretching vibrations, respectively [24,37,41,51]. Thus, the FT-IR spectra, besides the XPS results, provide further evidence for the bonding of B atoms to the graphene lattice.

Fig. 2e show the  $N_2$  adsorption-desorption isotherms of the samples. As can be seen, they exhibited a typical type IV isotherm, and the adsorption at low relative pressure ( $P/P_0 < 0.1$ ) indicates the presence of micropores ( $< 2\text{ nm}$ ) in the material [35]. The hysteresis loop at  $0.4 < P/P_0 < 1$  shows the presence of mesopores (2–50 nm). That is, the prepared materials have a hierarchical porous structure from micropores to macropores [49], which is evident in the pore distribution diagram in Fig. 2f. To quantify the pore size distribution, the Barrett-Joyner-Halenda (BJH) method and the Horvath-Kawazoe (H-K) method were used to analyze the size distribution of mesopores and micropores, respectively (Fig. 2f, inset). In carbon materials, micropores provide abundant active sites for the ORR, leading to high  $H_2O_2$  yield [52–55], while mesopores serve as gas channels to supply oxygen [53]. As shown in Fig. 2e and 2f, the mesopores and micropores of the samples increased with increasing B dopant, and the specific surface area increased accordingly. This was supported by electrochemical measurements of the catalysts, which showed that the EDLC of B-doped rGO was larger than that of rGO (Fig. 2g, Fig. S6 and S7). In addition, EIS measurements show that B-doping enhances the charge transfer of rGO (Fig. 2h and 2i).

Subsequently, the  $2e^-$  ORR selectivity of the prepared samples was investigated. Measurements were performed under neutral (pH 6.5) and acidic (pH 3.0) media. As can be seen from Fig. 3a, 3b, Fig. S8 and S9, B-doped rGO showed a higher onset potential and larger current response compared to rGO, demonstrating enhanced  $2e^-$  ORR activity. The calculated  $e^-/O_2$  values (Fig. 3c and 3d) showed that B-doping enhances  $H_2O_2$  selectivity, and the  $H_2O_2$  selectivity increased with increasing B dopant. For 4B-rGO-800, the  $e^-/O_2$  value approaches 2 in both neutral and acidic media. However, when the B dopant further increased, both of its selectivity and activity obviously decreased (Fig. 3a-3d and Fig. S9). Almost the same results were observed in the measurements using RRDE (Fig. S10).

To further confirm the  $2e^-$  ORR performance of the B-doped rGO, the  $H_2O_2$  yield and current efficiency of the catalysts modified GDE were compared. The  $H_2O_2$  accumulation of different catalysts modified GDE at a current density of  $60\text{ mA cm}^{-2}$  was shown in Fig. 3e. The  $2e^-$  ORR activity of carbon cloth without catalyst was very low and its  $H_2O_2$  accumulation was only  $0.77\text{ mg cm}^{-2}\text{ h}^{-1}$  (Fig. 3e). The  $H_2O_2$  yield and current efficiency of B-doped rGO gradually increased with the increasing of B dopant, and the  $H_2O_2$  accumulation of 4B-rGO-800 reached the highest value of  $30.24\text{ mg cm}^{-2}\text{ h}^{-1}$  (corresponding current efficiency of 79.45%, Fig. 3f), which was 49.5% higher than that of rGO. However, when the B dopant increased further, the  $H_2O_2$  yield decreased. The  $H_2O_2$  accumulation and current efficiency of rGO and 4B-rGO-800 at different current density and pH values were shown in Fig. 3g and 3h, respectively. As shown in Fig. 3g, the current efficiency tended to decrease with increasing current density, which may be due to side reactions such as decomposition of generated  $H_2O_2$ . In addition, B-doped rGO exhibited excellent  $H_2O_2$  yield and current efficiency in all measured pH ranges (Fig. 3h). Based on the experimental results, it can

be preliminarily concluded that B doping enhances the  $2e^-$  ORR performance of rGO and the performance of B-doped rGO was dependent on the B content.

To investigate the effect of OFGs and defects on the  $2e^-$  ORR performance of B-doped rGO, B-doped rGO catalysts with different oxygen content and defects were prepared and their  $2e^-$  ORR performance was compared. The annealing temperature of the samples was determined based on the TGA results of the as-prepared aerogels (Fig. S11) [44]. The Raman spectra of different samples showed that the defects in B-doped rGO significantly increased with increasing annealing temperature (Fig. S12). To accurately investigate the defect of the samples, we deconvoluted the Raman spectra into five bands (Fig. 4a) [49]. As shown in Fig. 4a and Table S2, the  $I_{D1}/I_G$  and  $I_{D4}/I_G$  of B-doped rGO obviously increased with the increase of annealing temperature, indicating that defects in the material were increased with increasing annealing temperature [49]. The XPS spectra (Fig. 4b, 4c, Fig. S13, and S14) showed that the O content of samples decreased to 5.69%, 3.75%, 3.38%, and 2.83%, respectively, as increasing annealing temperature, while the B content ranged from 0.91% to 1.12%, and the ratio of different B species did not change significantly (Fig. 4b). Conversely, as can be seen from Fig. 4c, the ratio of different OFGs changed with the annealing temperature.

Meanwhile, the electrochemical measurements showed that the charge transfer resistance ( $R_{ct}$ ) of B-doped rGO increased firstly and then decreased again with increasing annealing temperature (Fig. 4d and 4e), and the EDLC of the materials decreased significantly (Fig. 4f and Fig. S16). These results indicate that the increase of annealing temperature increased the defect content of B-doped rGO and caused the decrease of OFG content and EDLC.

Subsequently, the  $2e^-$  ORR performance of the catalysts at different annealing temperatures were evaluated. As shown in Fig. 5a, 5b and Fig. S17, the  $e^-/O_2$  values of different catalysts were all close to 2 and there was no significant difference among them. However, the ORR activity of 4B-rGO-900 significantly decreased due to its low electrochemical active surface area (ECSA) (Fig. 4f).

Similar results were observed in the  $H_2O_2$  accumulation experiments in Fig. 5c. The  $H_2O_2$  yields and current efficiencies of the different catalysts ranged from  $28.8$  to  $30.24\text{ mg cm}^{-2}\text{ h}^{-1}$  and from 75.7% to 79.4%, respectively, with no significant differences among them. These results lead to the conclusion that the  $2e^-$  ORR performance of B-doped rGO were mainly determined by the doped B element and that OFGs or defects did not play a significant role in the  $2e^-$  ORR activity of B-doped rGO.

### 3.2. Effect of oxygen content of cathode gas on ORR performance of catalysts

In the ORR, as in any chemical reaction, the mass transfer of reactants is an important factor, and in particular, oxygen mass transfer has a strong influence on the  $2e^-$  ORR [15–17]. To study the effect of oxygen content of cathode gas on the ORR performance of B-doped rGO, a series of experiments were conducted. Firstly, the ORR performance changes of different catalysts in an air atmosphere were investigated using the modified H-cell (Fig. 6a-e, Fig. S18, and S19). The oxygen content of the laboratory atmosphere was measured to be  $20.87 \pm 0.18\%$ . As shown in Fig. 6a and 6b, the ORR activity of 4B-rGO-800 catalyst exhibits a significant difference between oxygen and air atmosphere, and its current response during LSV differed by almost fourfold. The same results were observed for other catalysts (Fig. S8, S9, S18 and S19). It is noteworthy that not only the ORR activity of the catalysts decreased in the air atmosphere, but also the  $H_2O_2$  selectivity of the catalyst decreased significantly (Fig. 6c and 6d). That is, as the cathode potential was scanned negatively, the  $H_2O_2$  selectivity of the catalysts began to gradually decrease, and the  $e^-/O_2$  value increased from the initial 2.2–2.3 to 3.3–3.5. The oxygen consumption at the cathode during the measurement period was approximately 6–10  $\mu\text{mol}$  (Fig. S18 and

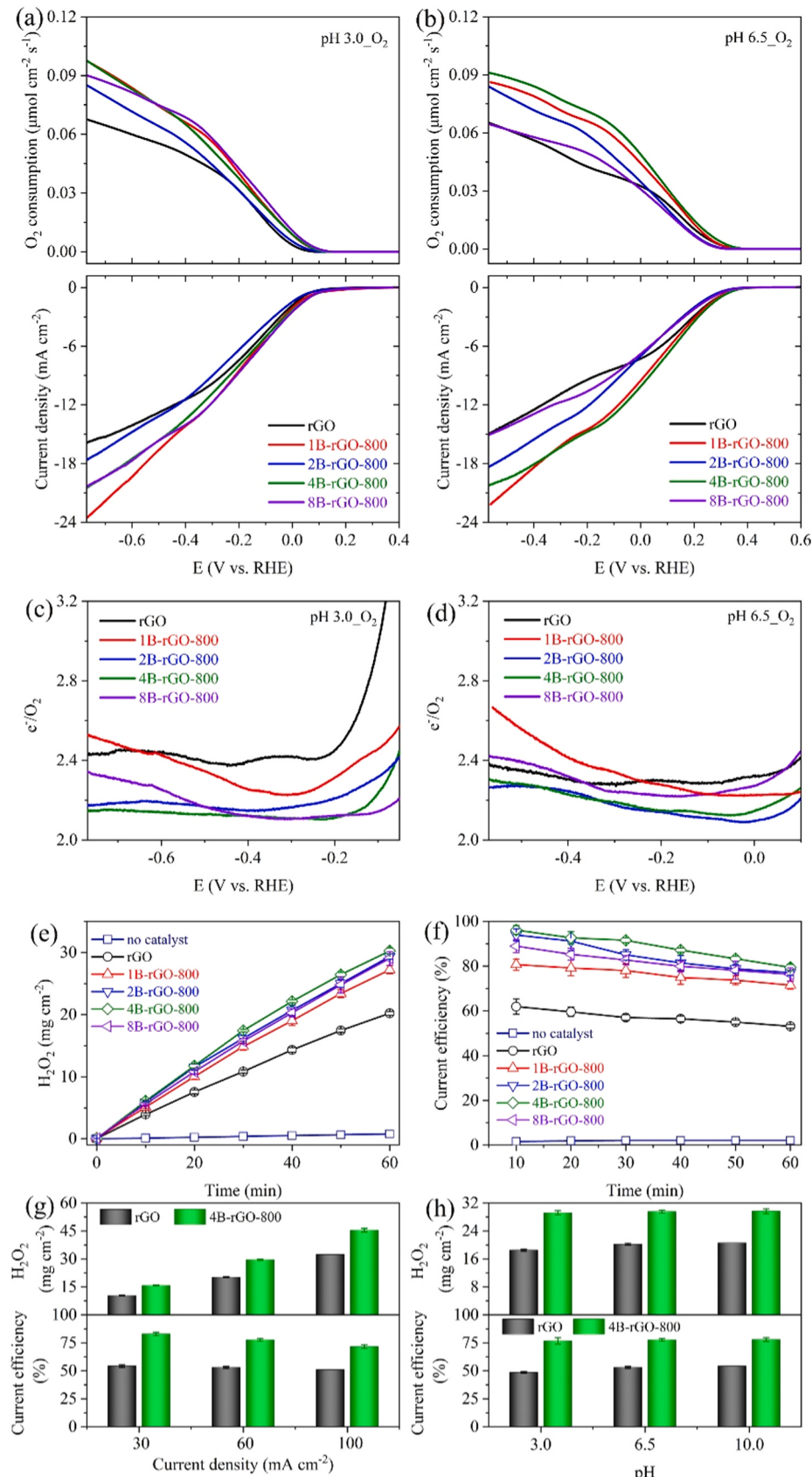


**Fig. 3.** Oxygen consumption measurement of rGO, 1B-rGO-800, 2B-rGO-800, 4B-rGO-800 and 8B-rGO-800 during LSV at (a) pH 3, (b) pH 6.5, the corresponding  $e^-/O_2$  at (c) pH 3.0, and (d) pH 6.5 (catalyst loading mass: 200  $\mu\text{g cm}^{-2}$ , scan rate: 1 mV s<sup>-1</sup>). (e) The  $\text{H}_2\text{O}_2$  accumulation and (f) corresponding current efficiency of rGO, 1B-rGO-800, 2B-rGO-800, 4B-rGO-800 and 8B-rGO-800 (current density: 60  $\text{mA cm}^{-2}$ ; pH 6.5), and (g) effects of applied current density and (h) electrolyte pH on  $\text{H}_2\text{O}_2$  accumulation and current efficiency of rGO and 4B-rGO-800 (catalyst loading mass: 3  $\text{mg cm}^{-2}$ ).

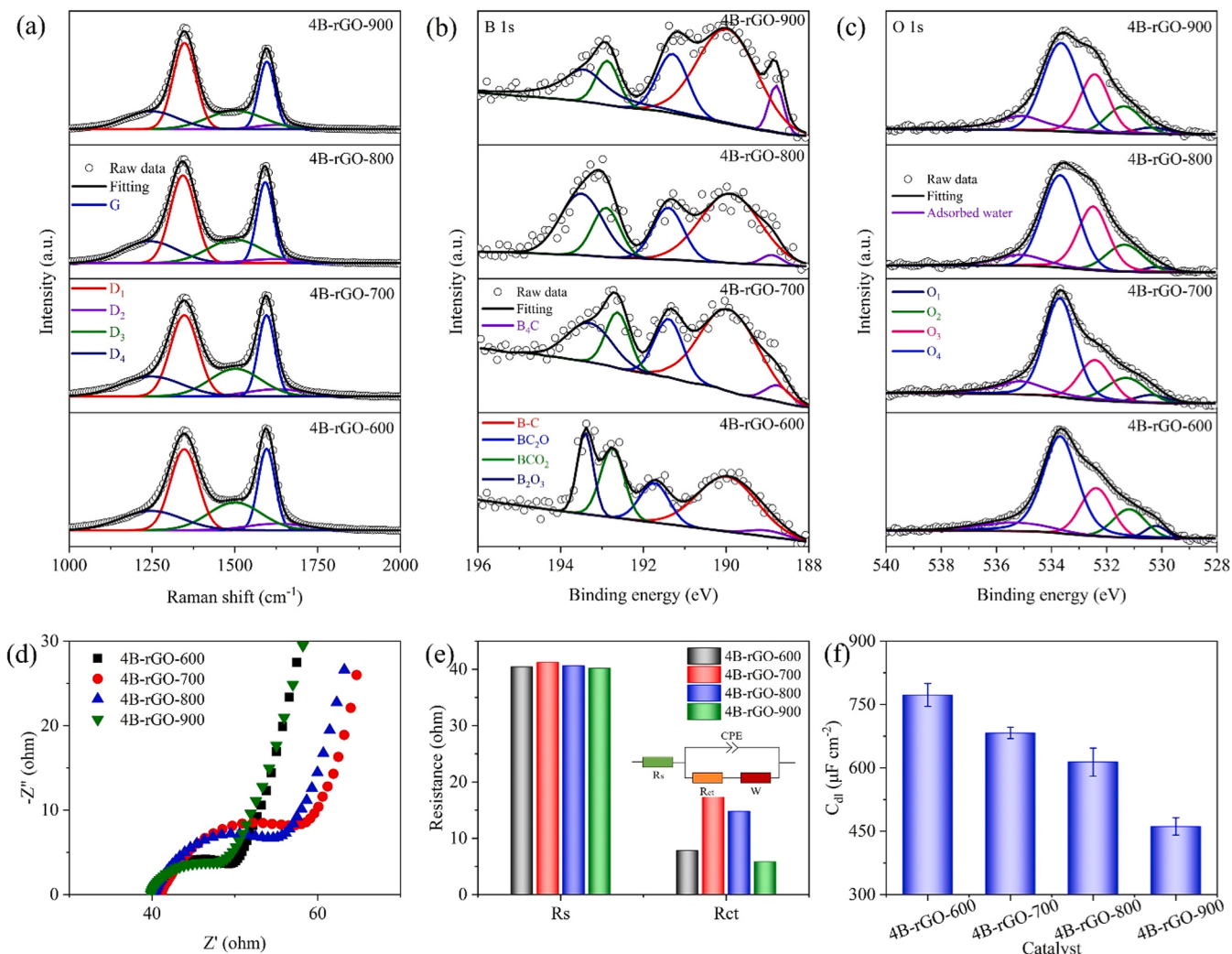


**Fig. 4.** Deconvoluted (a) Raman spectra, (b) XPS B1s spectra, and (c) XPS O1s spectra of 4B-rGO-600, 4B-rGO-700, 4B-rGO-800 and 4B-rGO-900. (d) Nyquist plots, (e) the corresponding ohmic resistance and charge-transfer resistance, and (f) EDLC of 4B-rGO-600, 4B-rGO-700, 4B-rGO-800 and 4B-rGO-900 (catalyst loading mass:  $100 \mu\text{g cm}^{-2}$ ).

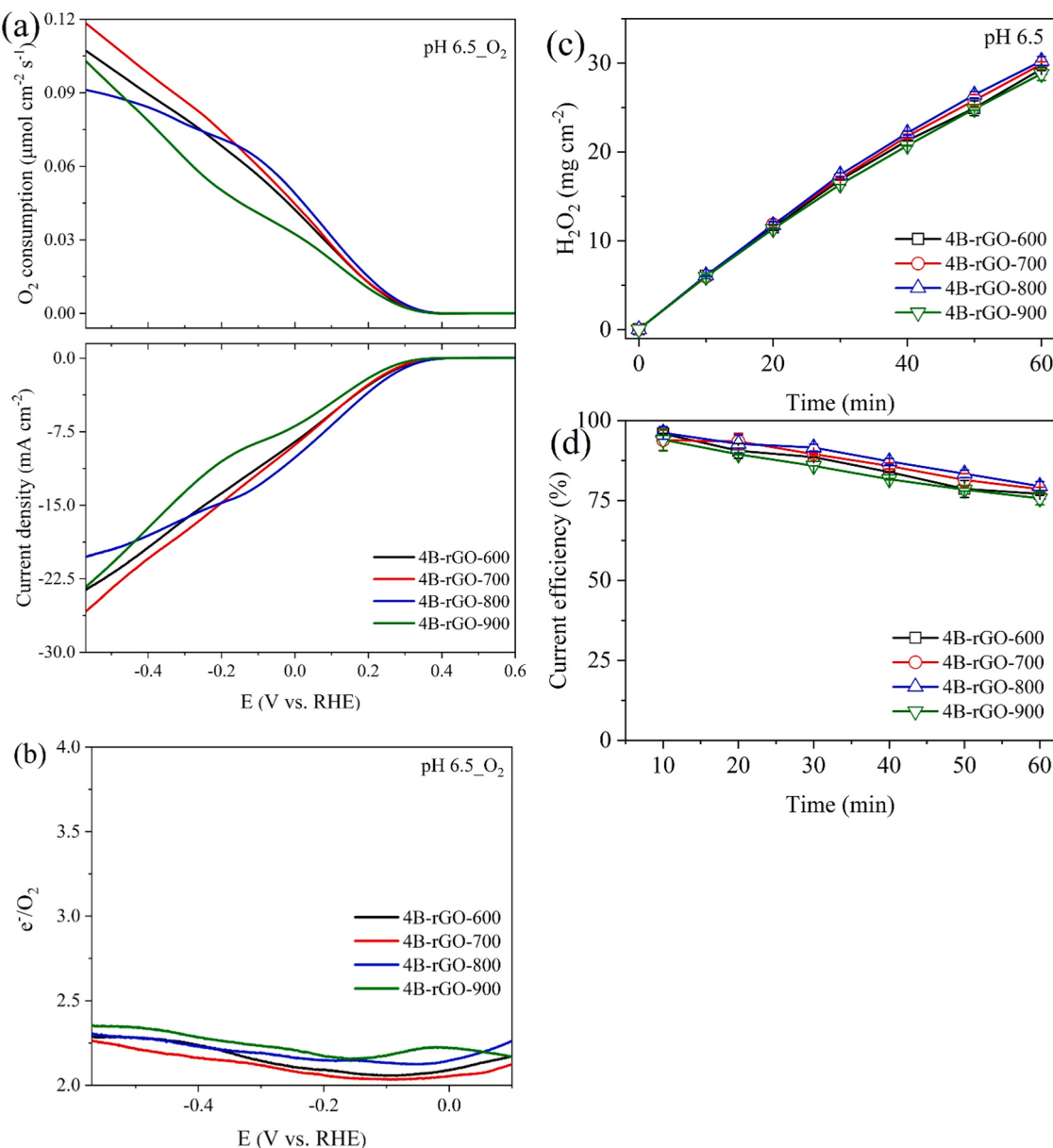
S19), which converted to a change in oxygen content in the cathode chamber of only 0.74–1.23%. Thus, the impact of the change in oxygen content could be neglected. These results were also confirmed by CP measurements in the modified H-cell. In oxygen atmosphere, the 4B-rGO-800 catalyst exhibited high  $\text{H}_2\text{O}_2$  selectivity with an average  $\text{e}^-/\text{O}_2$  value of 1.99 during the measurement period (60 min) at a current density of  $3 \text{ mA cm}^{-2}$ . These results closely match the current efficiency of 97.2% (equivalent to 98.6% when converted to  $2\text{e}^-$  ORR selectivity [56]) calculated from its  $\text{H}_2\text{O}_2$  accumulation (Fig. 6f and Fig. S20). In contrast, the  $\text{H}_2\text{O}_2$  selectivity decreased significantly in air atmosphere (Fig. 6g). The results showed that low oxygen content of cathode gas during the ORR leads to a decrease in the  $2\text{e}^-$  ORR selectivity (due to oxygen mass transfer limitation), and this trend was intensified with increasing current density (Fig. S21). These results confirmed the importance of oxygen mass transfer in the ORR and suggested that increasing the oxygen content of the cathode gas will possibly improve the  $\text{H}_2\text{O}_2$  yield and current efficiency. Therefore, the  $\text{H}_2\text{O}_2$  yield and current efficiency were investigated by improving the oxygen content of the gas supplied to the B-doped rGO modified GDE, in which the oxygen content of the gas was  $20.87 \pm 0.18\%$  (pristine air),  $30 \pm 0.5\%$ ,  $40 \pm 0.5\%$  and nearly 100%, respectively.

Fig. 6h and 6i show the  $\text{H}_2\text{O}_2$  yield and current efficiency at different oxygen content when the current density was  $200 \text{ mA cm}^{-2}$ . At 30%

oxygen content, the  $\text{H}_2\text{O}_2$  yield was  $84.3 \text{ mg cm}^{-2} \text{ h}^{-1}$ , which was 14.5% higher than that of pristine air, and when the oxygen content reached to 40%, the  $\text{H}_2\text{O}_2$  yield reached  $94.6 \text{ mg cm}^{-2} \text{ h}^{-1}$  and the current efficiency was 74.57%, which were 28.5% higher than those of pristine air. These values were almost the same as those of pure oxygen ( $95.63 \text{ mg cm}^{-2} \text{ h}^{-1}$ , 75.36%), which means that increasing the oxygen content of the gas supplied to the B-doped rGO modified GDE can significantly improve its  $\text{H}_2\text{O}_2$  yield and current efficiency, and this effect becomes more obvious as the current density increases (Fig. 6j). This demonstrates that when the B-doped rGO modified GDE is applied to the EF process, it is not necessary to use expensive pure oxygen to improve its  $\text{H}_2\text{O}_2$  yield, and oxygen-enriched air with an oxygen content of 30–40% can achieve the same effect as pure oxygen. Currently, oxygen-enriched air with an oxygen content of 25–40% can be obtained relatively simply and cheaply by membrane separation technology or pressure swing adsorption (PSA) and has been applied in various industrial applications [57,58]. These results suggest new possibilities for scaling up B-doped rGO modified GDE and the EF technology to industrial scale.

### 3.3. Mechanism exploration

To investigate the active site of B-doped rGO and to describe its ORR



**Fig. 5.** (a) Oxygen consumption measurement of 4B-rGO-600, 4B-rGO-700, 4B-rGO-800 and 4B-rGO-900 during LSV at pH 6.5, and (b) the corresponding  $e^-/O_2$  (catalyst loading mass: 200  $\mu\text{g cm}^{-2}$ ; scan rate: 1  $\text{mV s}^{-1}$ ). (c) The  $\text{H}_2\text{O}_2$  accumulation and (d) corresponding current efficiency of 4B-rGO-600, 4B-rGO-700, 4B-rGO-800 and 4B-rGO-900 (catalyst loading mass: 3  $\text{mg cm}^{-2}$ ; current density: 60  $\text{mA cm}^{-2}$ ; pH 6.5).

mechanism, a series of experiments were designed and conducted. The study in Section 3.2 has demonstrated that the 2e<sup>-</sup> ORR selectivity of B-doped rGO can be changed with the oxygen content of cathode gas. Therefore, by filling the cathode chamber of the modified H-cell with air and conducting CP measurements, the oxygen content in the cathode chamber will gradually decrease as the oxygen is consumed at the cathode, as a result, it is possible to induce a change in the ORR pathway. To determine the initial amount of oxygen in the cathode chamber, the cathode chamber air volume was obtained from the volume expansion method and the ideal gas law (Eq. (S1)), and the air volume of the cathode chamber was  $19.89 \pm 0.25$  mL when the electrolyte was 36 mL. Fig. 7a, Fig. S21 and S22 show the CP measurements (current density of 1  $\text{mA cm}^{-2}$ ) of different catalysts. When the oxygen content was above 10%, the  $e^-/O_2$  values of the catalysts were between 2 and 2.5, which generally follow the two-electron pathway. At this time, the electrode potentials of both 4B-rGO-800 and 8B-rGO-800 were more than 40–70 mV higher than that of rGO, indicating that B-doped rGO has

a smaller overpotential than rGO. When the oxygen content reached 9.4% and 8.2%, respectively, the  $e^-/O_2$  values of rGO and 4B-rGO-800 increased rapidly to 4, and at this time, the electrode potential also dropped rapidly by more than 150–170 mV. In other words, the ORR transitioned from the two-electron pathway to the four-electron pathway, and this required a relatively high overpotential. In contrast, the change of 8B-rGO-800 electrode potential during the transition to the four-electron pathway was not significant (Fig. 7a), and the electrode potential during the 4e<sup>-</sup> ORR was more than about 150 mV higher than that of 4B-rGO-800. These results indicate that the 8B-rGO-800 catalyst has active sites capable of catalyzing the 4e<sup>-</sup> ORR that were absent or very poor in 4B-rGO-800.

To investigate the 2e<sup>-</sup> ORR active site in B-doped rGO and to understand its ORR mechanism, DFT calculations were performed. The study in Section 3.1 has demonstrated that the selectivity of B-doped rGO was related to the content of B dopant (Fig. 7b and 7c). Consequently, models constructed based on doped B species as shown in

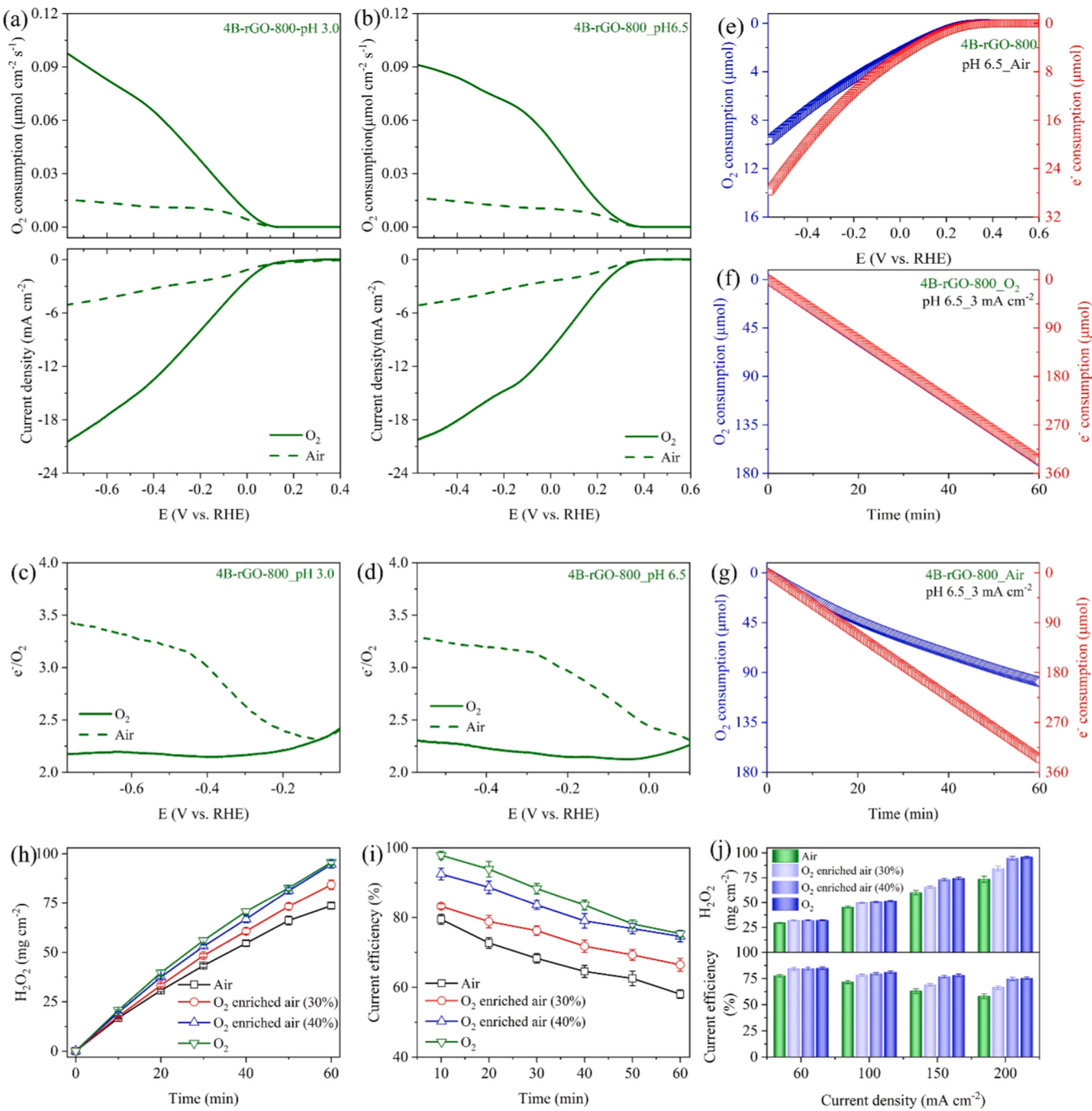


**Fig. 6.** Oxygen consumption measurement of 4B-rGO-800 during LSV in the oxygen and air atmosphere at (a) pH 3.0, (b) pH 6.5, the corresponding  $e'/O_2$  at (c) pH 3.0, and (d) pH 6.5 (catalyst loading mass:  $200 \mu\text{g cm}^{-2}$ ; scan rate:  $1 \text{ mV s}^{-1}$ ). (e) Simultaneous and direct measurement of total  $e^-$  and  $O_2$  moles consumed during LSV of 4B-rGO-800 in air atmosphere. Simultaneous and direct measurement of total  $e^-$  and  $O_2$  moles consumed during chronopotentiometry of 4B-rGO-800 in (f) oxygen and (g) air atmosphere. (h) The  $H_2O_2$  accumulation and (i) corresponding current efficiency of 4B-rGO-800 modified GDE at different oxygen contents (catalyst loading mass:  $3 \text{ mg cm}^{-2}$ ; current density:  $200 \text{ mA cm}^{-2}$ ; pH 6.5). (j) Effects of oxygen contents on  $H_2O_2$  accumulation and current efficiency of 4B-rGO-800 at different current density.

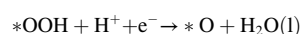
Fig. 7d, and the reaction energy barrier of the possible active sites to the  $^*OOH$  intermediate was calculated (Fig. 7e). In the  $2e^-$  ORR process, the  $O_2$  molecule is firstly adsorbed on the active site and then reduced to  $^*OOH$  via hydrogenation reaction (Eq. (3)). The next second electron transfer results in the reduction of  $^*OOH$  and the generation of  $H_2O_2$  (Eq. (4)) [3,5,35].



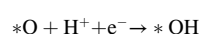
(3)



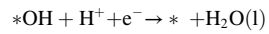
(4)



(5)



(6)



(7)

The reaction kinetics and pathway of ORR depends on the reaction

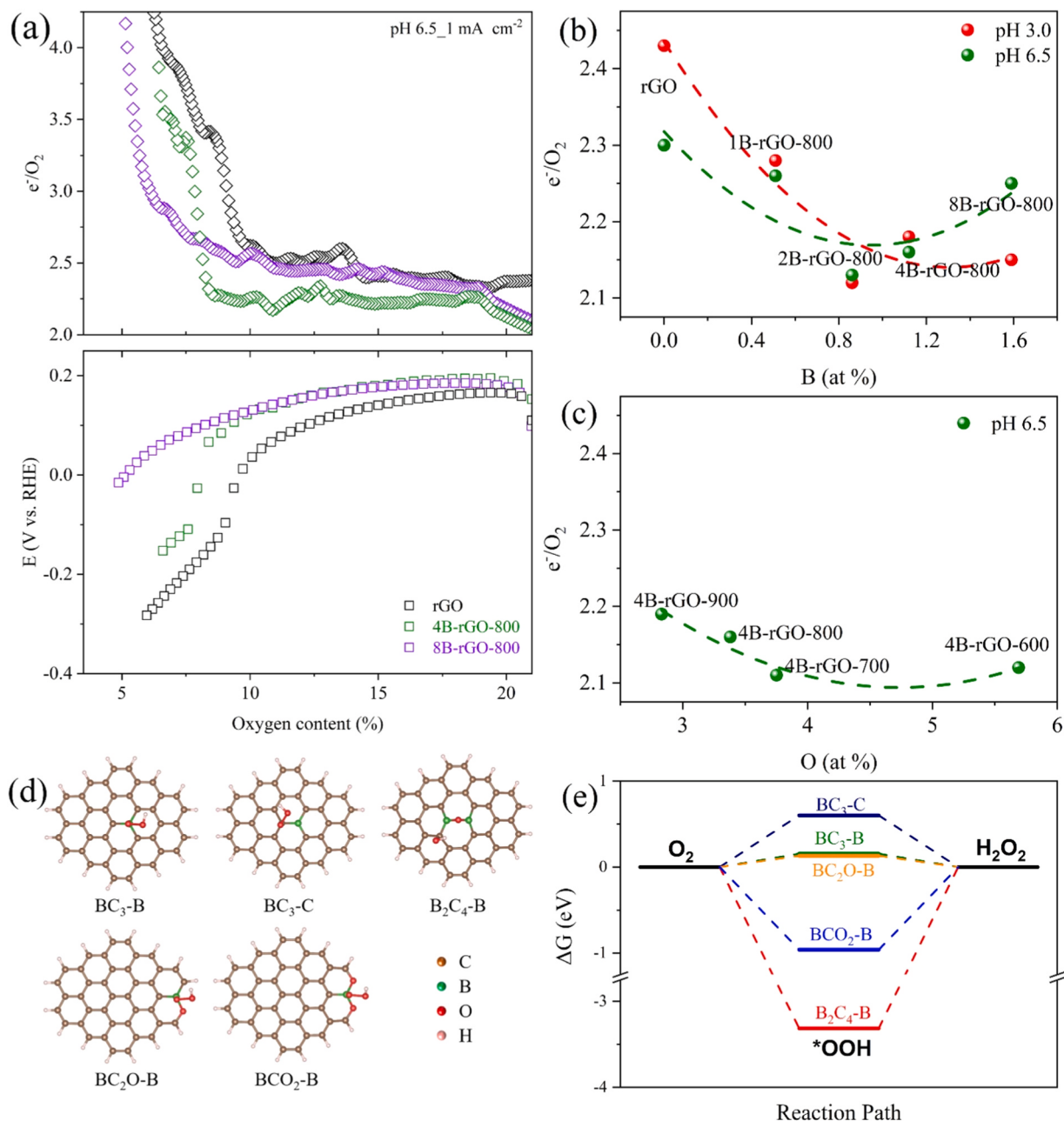


**Fig. 7.** (a) Variation of  $e^-/O_2$  with oxygen content during CP measurement of rGO, 4B-rGO-800, and 8B-rGO-800 (catalyst loading mass:  $200 \mu\text{g cm}^{-2}$ ; electrode area:  $3 \text{ cm}^2$ ; current density:  $1 \text{ mA cm}^{-2}$ ). Relationship between the  $e^-/O_2$  and (b) amount of boron, (c) amount of oxygen. (d) The optimized models with  $^*OOH$  intermediates adsorption. (e) The illustration of  $2e^-$  ORR reaction pathway on the optimized models.

energy barrier ( $\Delta G$ ) from  $O_2$  to  $^*OOH$  [11,12], and in an idealized model, the reaction free energy of all electron transfer steps should be zero when the applied potential is equal to the equilibrium potential [11, 14,59,60]. As shown in Fig. 7e, the  $\Delta G$  of  $BC_2O-B$  and  $BC_3-B$  were closest to zero of  $0.131 \text{ eV}$  and  $0.156 \text{ eV}$ , respectively, suggesting that these two species of B-atoms act as the active sites for the  $2e^-$  ORR of B-doped rGO. Moreover, the  $\Delta G$  of  $BC_3-C$  and  $BCO_2-B$  were  $0.603 \text{ eV}$  and  $-0.961 \text{ eV}$ , which requires a relatively large overpotential to catalyze  $2e^-$  ORR. Importantly, the  $\Delta G$  of the interconnected B atom,  $B_2C_4-B$ , was  $-3.314 \text{ eV}$ , and the bond with the  $^*OOH$  intermediate was so strong that the O-O bond was broken and decomposed to  $^*O$  intermediate in the next steps of the ORR (Eq. (5–7)). That is,  $B_2C_4-B$  was the active site to catalyze the  $4e^-$  ORR, and the ratio of interconnected B atoms such as  $B_2C_4$  increases with increasing B content [37,43], which is in good agreement with the experimental results shown in Section 3.1 and

Fig. 7a, where the  $H_2O_2$  selectivity decreases with the increase of boron content.

#### 3.4. Stability test and continuous degradation of organic pollutants

Besides high ORR performance, the stability of the catalyst is also very important. To investigate the stability of B-doped rGO, long-term tests were performed using catalyst modified carbon paper electrodes and GDEs. Firstly, CP measurements were performed using the 4B-rGO-800 modified carbon paper electrode for two cycles of  $6 \text{ h}$  at a current density of  $5 \text{ mA cm}^{-2}$ . As can be seen from Fig. 8a, the electrode potential tended to decrease slightly with the reaction time, however, it recovered to the initial value at the second measurement, and the current efficiency was consistently maintained during the measurement period ( $12 \text{ h}$ ) and reached an average of  $95.6\%$  (Fig. 8a and Fig. S23). To

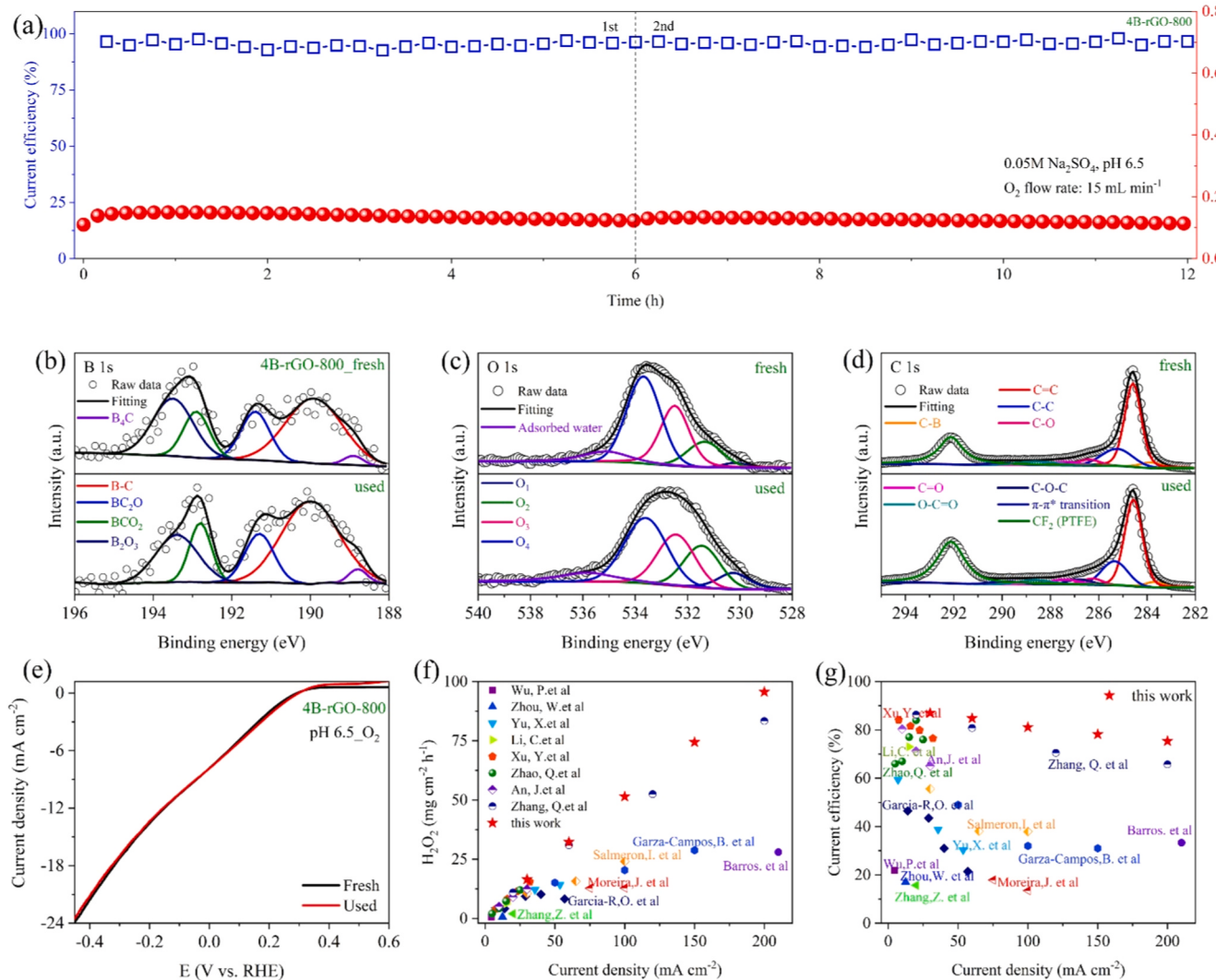


**Fig. 8.** (a-e) B-doped rGO's stability test results and (f, g) ORR performance comparison with the literature. (catalyst loading mass:  $200 \mu\text{g cm}^{-2}$ ; current density:  $5 \text{ mA cm}^{-2}$ ;  $\text{O}_2$  flow rate:  $15 \text{ mL min}^{-1}$ ; pH: 6.5).

further confirm the stability of the B-doped rGO, XPS analysis was performed on the electrodes before and after CP measurements. As shown in the high-resolution XPS spectra in Fig. 8b, 8c, 8d, and Fig. S24, the B content and ratio of B species in 4B-rGO-800 before and after the ORR showed no significant difference. However, there was a change in the ratio of the various OFGs (Fig. 8c). Nevertheless, as shown in Section 3.1, the effect of OFGs on the  $2\text{e}^-$  ORR activity of B-doped rGO was very small. This demonstrated the excellent stability of the B-doped rGO catalyst, which was also confirmed by the LSV measurement of the electrode after the CP measurements (Fig. 8e).

Additionally, the ORR performance of B-doped rGO was compared with previous studies. As can be seen from Fig. 8f and 8g, most of the studies on  $2\text{e}^-$  ORR focused on low current densities below  $50 \text{ mA cm}^{-2}$ , and the  $\text{H}_2\text{O}_2$  yield and current efficiency were insufficient at high current densities above  $100 \text{ mA cm}^{-2}$ . In contrast, B-doped rGO maintains a high  $\text{H}_2\text{O}_2$  yield of  $95.63 \text{ mg cm}^{-2} \text{ h}^{-1}$  and a current efficiency of 75.36% even at a high current density of  $200 \text{ mA cm}^{-2}$ .

Subsequently, the experiments were conducted to continuously degrade organic pollutants using the B-doped rGO modified GDE. The degradation experiments were conducted continuously for 5–7 h at different oxygen content of the gas supplied to B-doped rGO modified GDE (Fig. 9, Fig. S25–S29). Firstly, as can be seen from Fig. 9, Fig. S26, S28, and S30, the  $\text{H}_2\text{O}_2$  yields of the B-doped rGO modified GDE at

different oxygen content (pristine air, 30%, 40%) were  $28.22$ ,  $30.63$ , and  $31.11 \text{ mg cm}^{-2} \text{ h}^{-1}$ , respectively, and the current efficiencies were 73.9%, 79.9%, and 81.4%, respectively. These results confirmed the high stability of the B-doped rGO and the effectiveness of the oxygen-enriched air. As shown in Fig. 9 and Fig. S28, the degradation rates of more than 99% were achieved for three target pollutants (RhB, AAP and TC) in the continuous degradation experiments. However, in the case of IOH, its degradation rate was slightly lower than that of other pollutants, was 91.22% at an initial concentration of  $80 \text{ mg L}^{-1}$  and 86.1% at  $160 \text{ mg L}^{-1}$  (Fig. 9a and Fig. S31). To investigate the mineralization capability of the homogeneous EF system, its TOC removal rates were measured, and the results showed that a minimum of 17% (initial concentration of  $160 \text{ mg L}^{-1}$ ) and a maximum of 34.3% (initial concentration of  $5 \text{ mg L}^{-1}$ ) TOC removal rates were achieved for RhB degradation (Fig. S32). Unfortunately, the TOC removal rate for AAP was only 1–3.5%, as shown in Fig. 9b and Fig. S33.

Interestingly, the TOC removal rate increased with increasing initial concentration of TC during degradation (Fig. 9c and Fig. S34). It can be speculated that due to the structure of TC with dimethylamino ( $-\text{N}(\text{CH}_3)_2$ ), amide ( $-\text{CONH}_2$ ) and amine group ( $-\text{NH}_2$ ), after binding with  $\text{Fe}^{3+}$ , the electron transfer of TC induced the reduction of  $\text{Fe}^{3+}$ , thus accelerating the cycle of Fe [61]. These results show that B-doped rGO has improved  $2\text{e}^-$  ORR activity and high stability, so it is expected that it

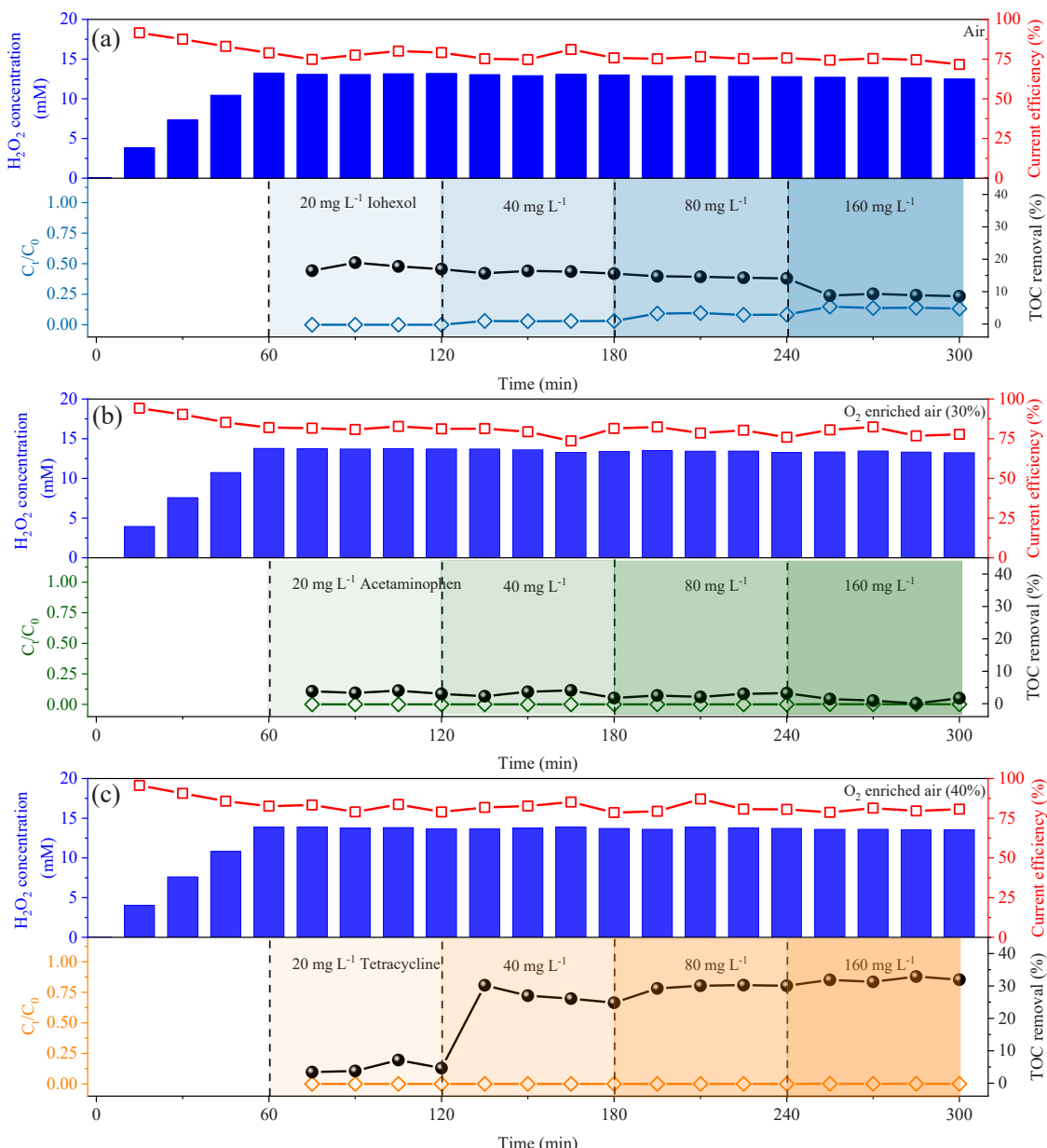


**Fig. 9.** Continuous degradation experiments of (a) IOH, (b) AAP, and (c) TC in a homogeneous EF system using 4B-rGO-800 modified GDE (catalyst loading mass: 3 mg cm<sup>-2</sup>; electrode area: 3 cm<sup>2</sup>; current density: 60 mA cm<sup>-2</sup>; pH: 3.0; Fe<sup>2+</sup>: 1 mM).

can be utilized in the EF process for actual wastewater treatment.

#### 4. Conclusion

In this study, B-doped rGO catalysts were successfully prepared and they exhibited a high selectivity of 95–98.6% for 2e<sup>-</sup> ORR, and the H<sub>2</sub>O<sub>2</sub> yield reached up to 95.63 mg cm<sup>-2</sup> h<sup>-1</sup> at a current density of 200 mA cm<sup>-2</sup>. Furthermore, the oxygen content of the gas supplied to the cathode significantly impacts both the ORR activity and selectivity of the B-doped rGO catalyst. It was observed that increasing the oxygen concentration in the gas supplied to the B-doped rGO modified GDE only to 30–40%, resulted in almost the same H<sub>2</sub>O<sub>2</sub> yield as using pure oxygen within the experimental range (current density of 60–200 mA cm<sup>-2</sup>). The experimental analysis and DFT calculations demonstrate that isolated B atoms, including BC<sub>2</sub>O-B and BC<sub>3</sub>-B, act as active sites for 2e<sup>-</sup> ORR in B-doped rGO, whereas interconnected B atoms, such as B<sub>2</sub>C<sub>4</sub>-B, catalyze the 4e<sup>-</sup> ORR. Finally, B-doped rGO modified GDE was utilized to construct a homogeneous electro-Fenton system for the continuous

degradation of recalcitrant organic pollutants. Thus, the high performance of the B-doped rGO renders it a viable alternative catalyst in the electro-Fenton process.

#### CRediT authorship contribution statement

**KwangChol Ri:** Conceptualization, Methodology, Investigation, Writing – original draft, Validation, Formal analysis, Visualization, Software. **SongSik Pak:** Data curation, Investigation. **Dunyu Sun:** Data curation, Investigation. **Qiang Zhong:** Data curation, Investigation. **Shaogui Yang:** Resources, Writing – review & editing, Funding acquisition. **SongIl Sin:** Data curation, Software. **Leliang Wu:** Data curation, Investigation. **Yue Sun:** Data curation. **Hui Cao:** Data curation. **Chunxiao Han:** Data curation. **Chenmin Xu:** Resources, Writing – review & editing. **Yazi Liu:** Writing – review & editing. **Huan He:** Resources, Funding acquisition. **Shiyin Li:** Resources, Funding acquisition. **Cheng Sun:** Resources, Writing – review & editing.

## Declaration of Competing Interest

The authors declare that they have no known competing financial interests or personal relationships that could have appeared to influence the work reported in this paper.

## Data Availability

Data will be made available on request.

## Acknowledgments

This work was supported by the High-end Foreign Expert Introduction Program (G2023014055L), Major Projects of Jiangsu Provincial Department of Education (23KJA180004) and the “Kuncheng Talent” Science and Technology Innovation and Entrepreneurship Leading Talents Program in Changshu.

## Appendix A. Supporting information

Supplementary data associated with this article can be found in the online version at [doi:10.1016/j.apcatb.2023.123471](https://doi.org/10.1016/j.apcatb.2023.123471).

## References

- [1] K.M. Nair, V. Kumaravel, S.C. Pillai, Carbonaceous cathode materials for electro-Fenton technology: mechanism, kinetics, recent advances, opportunities and challenges, *Chemosphere* 269 (2021), 129325.
- [2] S.O. Ganiyu, M. Zhou, C.A. Martínez-Huile, Heterogeneous electro-Fenton and photoelectro-Fenton processes: a critical review of fundamental principles and application for water/wastewater treatment, *Appl. Catal. B Environ.* 235 (2018) 103–129.
- [3] Y. Ding, W. Zhou, J. Gao, F. Sun, G. Zhao, H<sub>2</sub>O<sub>2</sub> Electrogeneration, from O<sub>2</sub> electroreduction by n-doped carbon materials: a mini-review on preparation methods, selectivity of N sites, and prospects, *Adv. Mater. Interfaces* 8 (2021) 2002091.
- [4] S. Yang, A. Verdaguera-Casadevall, L. Arnarson, L. Silvio, V. Colic, R. Frydendal, J. Rossmeisl, I. Chorkendorff, I.E.L. Stephens, Toward the decentralized electrochemical production of H<sub>2</sub>O<sub>2</sub>: a focus on the catalysis, *Acs Catal.* 8 (2018) 4064–4081.
- [5] J. Quílez-Bermejo, E. Morallón, D. Cazorla-Amorós, Metal-free heteroatom-doped carbon-based catalysts for ORR: a critical assessment about the role of heteroatoms, *Carbon* 165 (2020) 434–454.
- [6] E. Brillas, I. Sires, M.A. Oturan, Electro-fenton process and related electrochemical technologies based on fenton's reaction chemistry, *Chem. Rev.* 109 (2009) 6570–6631.
- [7] N. Thomas, D.D. Dionysiou, S.C. Pillai, Heterogeneous Fenton catalysts: a review of recent advances, *J. Hazard. Mater.* 404 (2021), 124082.
- [8] S. Gligorovski, R. Strelkowski, S. Barbati, D. Vione, Environmental implications of hydroxyl radicals (• OH), *Chem. Rev.* 115 (2015) 13051–13092.
- [9] Q. Zhu, Z. Pan, S. Hu, J.H. Kim, Cathodic hydrogen peroxide electrosynthesis using anthraquinone modified carbon nitride on gas diffusion electrode, *ACS Appl. Energy Mater.* 2 (2019) 7972–7979.
- [10] C. Li, C. Hu, Y. Song, Y.M. Sun, W. Yang, M. Ma, Active oxygen functional group modification and the combined interface engineering strategy for efficient hydrogen peroxide electrosynthesis, *ACS Appl. Mater. Interfaces* 14 (2022) 46695–46707.
- [11] Y.Y. Jiang, P.J. Ni, C.X. Chen, Y.Z. Lu, P. Yang, B. Kong, A. Fisher, X. Wang, Selective electrochemical H<sub>2</sub>O<sub>2</sub> production through two-electron oxygen electrochemistry, *Adv. Energy Mater.* 8 (2018) 1801909.
- [12] V. Viswanathan, H.A. Hansen, J. Rossmeisl, J.K. Norskov, Unifying the 2e<sup>-</sup> and 4e<sup>-</sup> reduction of oxygen on metal surfaces, *J. Phys. Chem. Lett.* 3 (2012) 2948–2951.
- [13] N. Wang, S. Ma, P. Zuo, J. Duan, B. Hou, Recent progress of electrochemical production of hydrogen peroxide by two-electron oxygen reduction reaction, *Adv. Sci.* 8 (2021), e2100076.
- [14] A. Kulkarni, S. Siahrostami, A. Patel, J.K. Norskov, Understanding catalytic activity trends in the oxygen reduction reaction, *Chem. Rev.* 118 (2018) 2302–2312.
- [15] Q.Z. Zhang, M.H. Zhou, G.B. Ren, Y.W. Li, Y.C. Li, X.D. Du, Highly efficient electrosynthesis of hydrogen peroxide on a superhydrophobic three-phase interface by natural air diffusion, *Nat. Commun.* 11 (2020) 1731.
- [16] F.J. Yin, Y. Liu, C. Wang, H. Liu, Assessing the electron transfer and oxygen mass transfer of the oxygen reduction reaction using a new electrode kinetic equation, *Phys. Chem. Chem. Phys.* 20 (2018) 16159–16166.
- [17] J. An, N. Li, Q. Zhao, Y. Qiao, S. Wang, C. Liao, L. Zhou, T. Li, X. Wang, Y. Feng, Highly efficient electro-generation of H<sub>2</sub>O<sub>2</sub> by adjusting liquid-gas-solid three phase interfaces of porous carbonaceous cathode during oxygen reduction reaction, *Water Res.* 164 (2019), 114933.
- [18] K.P. Gong, F. Du, Z.H. Xia, M. Durstock, L.M. Dai, Nitrogen-doped carbon nanotube arrays with high electrocatalytic activity for oxygen reduction, *Science* 323 (2009) 760–764.
- [19] Y. Xia, X.H. Zhao, C. Xia, Z.Y. Wu, P. Zhu, J.Y.T. Kim, X.W. Bai, G.H. Gao, Y.F. Hu, J. Zhong, Y.Y. Liu, H.T. Wang, Highly active and selective oxygen reduction to H<sub>2</sub>O<sub>2</sub> on boron-doped carbon for high production rates, *Nat. Commun.* 12 (2021) 4225.
- [20] P. Wu, Y. Zhang, Z. Chen, Y. Duan, Y. Lai, Q. Fang, F. Wang, S. Li, Performance of boron-doped graphene aerogel modified gas diffusion electrode for in-situ metal-free electrochemical advanced oxidation of Bisphenol A, *Appl. Catal. B Environ.* 255 (2019), 117784.
- [21] Y.A. Kim, K. Fujisawa, H. Muramatsu, T. Hayashi, M. Endo, T. Fujimori, K. Kaneko, M. Terrones, J. Behrends, A. Eckmann, C. Casiraghi, K.S. Novoselov, R. Saito, M. S. Dresselhaus, Raman spectroscopy of boron-doped single-layer graphene, *Acs Nano* 6 (2012) 6293–6300.
- [22] L. Yang, S. Jiang, Y. Zhao, L. Zhu, S. Chen, X. Wang, Q. Wu, J. Ma, Y. Ma, Z. Hu, Boron-doped carbon nanotubes as metal-free electrocatalysts for the oxygen reduction reaction, *Angew. Chem. Int. Ed.* 50 (2011) 7132–7135.
- [23] A.R. Jang, Y.W. Lee, S.S. Lee, J. Hong, S.H. Bae, S. Pak, J. Lee, H.S. Shin, D. Ahn, W.K. Hong, S. Cha, J.I. Sohn, I.K. Park, Electrochemical and electrocatalytic reaction characteristics of boron-incorporated graphene via a simple spin-on dopant process, *J. Mater. Chem. A* 6 (2018) 7351–7356.
- [24] X. Yu, P. Han, Z. Wei, L. Huang, Z. Gu, S. Peng, J. Ma, G. Zheng, Boron-doped graphene for electrocatalytic n2 reduction, *Joule* 2 (2018) 1610–1622.
- [25] T.V. Vineesh, M.P. Kumar, C. Takahashi, G. Kalita, S. Alwarappan, D. K. Pattanayak, T.N. Narayanan, Bifunctional electrocatalytic activity of boron-doped graphene derived from boron carbide, *Adv. Energy Mater.* 5 (2015) 1500658.
- [26] Z.H. Sheng, H.L. Gao, W.J. Bao, F.-B. Wang, X.H. Xia, Synthesis of boron doped graphene for oxygen reduction reaction in fuel cells, *J. Mater. Chem.* 22 (2012) 390–395.
- [27] Y. Zheng, J. He, S. Qiu, D. Yu, Y. Zhu, H. Pang, J. Zhang, Boosting hydrogen peroxide accumulation by a novel air-breathing gas diffusion electrode in electro-Fenton system, *Appl. Catal. B Environ.* 316 (2022), 121617.
- [28] Y. Li, H. Zhang, N. Han, Y. Kuang, J. Liu, W. Liu, H. Duan, X. Sun, Janus electrode with simultaneous management on gas and liquid transport for boosting oxygen reduction reaction, *Nano Res.* 12 (2019) 177–182.
- [29] H. Rabiee, L. Ge, X.Q. Zhang, S.H. Hu, M.R. Li, Z.G. Yuan, Gas diffusion electrodes (GDEs) for electrochemical reduction of carbon dioxide, carbon monoxide, and dinitrogen to value-added products: a review, *Energy Environ. Sci.* 14 (2021) 1959–2008.
- [30] W. Zhou, X. Meng, J. Gao, A.N. Alshawabkeh, Hydrogen peroxide generation from O<sub>2</sub> electroreduction for environmental remediation: a state-of-the-art review, *Chemosphere* 225 (2019) 588–607.
- [31] Q.Z. Zhang, M.H. Zhou, G.B. Ren, Y.W. Li, Y.C. Li, X.D. Du, Highly efficient electrosynthesis of hydrogen peroxide on a superhydrophobic three-phase interface by natural air diffusion, *Nat. Commun.* 11 (2020).
- [32] H.W. Kim, M.B. Ross, N. Kornienko, L. Zhang, J.H. Guo, P.D. Yang, B.D. McCloskey, Efficient hydrogen peroxide generation using reduced graphene oxide-based oxygen reduction electrocatalysts, *Nat. Catal.* 1 (2018) 282–290.
- [33] C. Xia, Y. Xia, P. Zhu, L. Fan, H.T. Wang, Direct electrosynthesis of pure aqueous H<sub>2</sub>O<sub>2</sub> solutions up to 20% by weight using a solid electrolyte, *Science* 366 (2019) 226–231.
- [34] H.W. Kim, V.J. Lukas, H. Park, S. Park, K.M. Diederichsen, J. Lim, Y.H. Cho, J. Kim, W. Kim, T.H. Han, J. Voss, A.C. Luntz, B.D. McCloskey, Mechanisms of two-electron and four-electron electrochemical oxygen reduction reactions at nitrogen-doped reduced graphene oxide, *Acs Catal.* 10 (2020) 852–863.
- [35] C. Li, C.Q. Hu, Y. Song, Y.M. Sun, W.S. Yang, M. Ma, Graphene-based synthetic fabric cathodes with specific active oxygen functional groups for efficient hydrogen peroxide generation and homogeneous electro-Fenton processes, *Carbon* 186 (2022) 699–710.
- [36] Z. Xing, W. Wang, X. Li, K. Zhang, L. Gan, Q. Wu, Electrochemical synthesis of hydrogen peroxide catalyzed by carbon nanotubes with surface Co-NX sites and encapsulated co nanoparticles, *ACS Appl. Mater. Interfaces* 14 (2022) 44282–44291.
- [37] T.V. Khai, H.G. Na, D.S. Kwak, Y.J. Kwon, H. Ham, K.B. Shim, H.W. Kim, Comparison study of structural and optical properties of boron-doped and undoped graphene oxide films, *Chem. Eng. J.* 211–212 (2012) 369–377.
- [38] W. Cermignani, T.E. Paulson, C. Onneby, C.G. Pantano, Synthesis and characterization of boron-doped carbons, *Carbon* 33 (1995) 367–374.
- [39] S. Jacques, A. Guette, X. Bodratt, F. Langlais, C. Guimon, C. Labrugere, L'PCVD and characterization of boron-containing pyrocarbon materials, *Carbon* 34 (1996) 1135–1143.
- [40] L.G. Jacobsohn, R.K. Schulze, M.E.H. Md Costa, M. Nastasi, X-ray photoelectron spectroscopy investigation of boron carbide films deposited by sputtering, *Surf. Sci.* 572 (2004) 418–424.
- [41] X. Mu, B. Yuan, X. Feng, S. Qiu, L. Song, Y. Hu, The effect of doped heteroatoms (nitrogen, boron, phosphorus) on inhibition thermal oxidation of reduced graphene oxide, *RSC Adv.* 6 (2016) 105021–105029.
- [42] F. Sun, Z. Qu, J. Gao, H.B. Wu, F. Liu, R. Han, L. Wang, T. Pei, G. Zhao, Y. Lu, In situ doping boron atoms into porous carbon nanoparticles with increased oxygen graft enhances both affinity and durability toward electrolyte for greatly improved supercapacitive performance, *Adv. Funct. Mater.* 28 (2018) 1804190.
- [43] T. Shirasaki, A. Derré, M. Ménétrier, A. Tressaud, S. Flandrois, Synthesis and characterization of boron-substituted carbons, *Carbon* 38 (2000) 1461–1467.

[44] D.Y. Yeom, W. Jeon, N.D.K. Tu, S.Y. Yeo, S.S. Lee, B.J. Sung, H. Chang, J.A. Lim, H. Kim, High-concentration boron doping of graphene nanoplatelets by simple thermal annealing and their supercapacitive properties, *Sci. Rep.* 5 (2015) 9817.

[45] F. Razmjoei, K.P. Singh, D.S. Yang, W. Cui, Y.H. Jang, J.S. Yu, Fe-Treated Heteroatom (S/N/B/P)-Doped Graphene Electrocatalysts for Water Oxidation, *AcS Catal.* 7 (2017) 2381–2391.

[46] A.B. Silva-Tapia, X. García-Carmona, L.R. Radovic, Similarities and differences in  $O_2$  chemisorption on graphene nanoribbon vs. carbon nanotube, *Carbon* 50 (2012) 1152–1162.

[47] A. Gabe, R. Ruiz-Rosas, E. Morallón, D. Cazorla-Amorós, Understanding of oxygen reduction reaction by examining carbon-oxygen gasification reaction and carbon active sites on metal and heteroatoms free carbon materials of different porosities and structures, *Carbon* 148 (2019) 430–440.

[48] G.L. Chai, Z. Hou, D.J. Shu, T. Ikeda, K. Terakura, Active sites and mechanisms for oxygen reduction reaction on nitrogen-doped carbon alloy catalysts: Stone-Wales defect and curvature effect, *J. Am. Chem. Soc.* 136 (2014) 13629–13640.

[49] C. Zhang, W. Liu, M. Song, J. Zhang, F. He, J. Wang, M. Xiong, J. Zhang, D. Wang, Pyranoid-O-dominated graphene-like nanocarbon for two-electron oxygen reduction reaction, *Appl. Catal. B Environ.* 307 (2022), 121173.

[50] G.F. Han, F. Li, W. Zou, M. Karamad, J.P. Jeon, S.W. Kim, S.J. Kim, Y. Bu, Z. Fu, Y. Lu, S. Siahrostami, J.B. Baek, Building and identifying highly active oxygenated groups in carbon materials for oxygen reduction to  $H_2O_2$ , *Nat. Commun.* 11 (2020) 2209.

[51] M. Sahoo, K.P. Sreena, B.P. Vinayan, S. Ramaprabhu, Green synthesis of boron doped graphene and its application as high performance anode material in Li ion battery, *Mater. Res. Bull.* 61 (2015) 383–390.

[52] A. Gabe, R. Ruiz-Rosas, C. González-Gaitán, E. Morallón, D. Cazorla-Amorós, Modeling of oxygen reduction reaction in porous carbon materials in alkaline medium. Effect of microporosity, *J. Power Sources* 412 (2019) 451–464.

[53] Y. Liu, K. Li, B. Ge, L. Pu, Z. Liu, Influence of micropore and mesoporous in activated carbon air-cathode catalysts on oxygen reduction reaction in microbial fuel cells, *Electrochim. Acta* 214 (2016) 110–118.

[54] M. Seredych, A. Szczerk, V. Fierro, A. Celzard, T.J. Bandosz, Electrochemical reduction of oxygen on hydrophobic ultramicroporous PolyHIPE carbon, *ACS Catal.* 6 (2016) 5618–5628.

[55] D. Barrera, M. Florent, M. Kulko, T.J. Bandosz, Ultramicropore-influenced mechanism of oxygen electroreduction on metal-free carbon catalysts, *J. Mater. Chem. A* 7 (2019) 27110–27123.

[56] C. Xia, J.Y. Kim, H.T. Wang, Recommended practice to report selectivity in electrochemical synthesis of  $H_2O_2$ , *Nat. Catal.* 3 (2020) 605–607.

[57] W. Bai, J. Feng, C. Luo, P. Zhang, H. Wang, Y. Yang, Y. Zhao, H. Fan, A comprehensive review on oxygen transport membranes: development history, current status, and future directions, *Int. J. Hydrol. Energy* 46 (2021) 36257–36290.

[58] N.F. Himma, A.K. Wardani, N. Prasetya, P.T.P. Aryanti, I.G. Wenten, Recent progress and challenges in membrane-based  $O_2/N_2$  separation, *Rev. Chem. Eng.* 35 (2019) 591–625.

[59] Q. Yuan, M. Fan, Y. Zhao, J. Wu, J. Raj, Z. Wang, A. Wang, H. Sun, X. Xu, Y. Wu, K. Sun, J. Jiang, Facile fabrication of carbon dots containing abundant h-BN/graphite heterostructures as efficient electrocatalyst for hydrogen peroxide synthesis, *Appl. Catal. B Environ.* 324 (2023), 122195.

[60] X. Li, X. Wang, G. Xiao, Y. Zhu, Identifying active sites of boron, nitrogen co-doped carbon materials for the oxygen reduction reaction to hydrogen peroxide, *J. Colloid Interface Sci.* 602 (2021) 799–809.

[61] Y. Deng, B. Zhang, C. Liu, F. Li, L. Fang, Z. Dang, C. Yang, Y. Xiong, C. He, Tetracycline-induced release and oxidation of As(III) coupled with concomitant ferrihydrite transformation, *Environ. Sci. Technol.* 56 (2022) 9453–9462.